Studies in Conservation

ISSN: (Print) (Online) Journal homepage: www.tandfonline.com/journals/ysic20

Mosaic Materials in an Art Deco Steel-framed Building

Grace A. Morris, Kevin Briggs, Michael Beare, Geoffrey Allen & Richard J. Ball

To cite this article: Grace A. Morris, Kevin Briggs, Michael Beare, Geoffrey Allen & Richard J. Ball (24 May 2024): Mosaic Materials in an Art Deco Steel-framed Building, Studies in Conservation, DOI: 10.1080/00393630.2024.2339711

To link to this article: https://doi.org/10.1080/00393630.2024.2339711

© 2024 The Author(s). Published by Informa UK Limited, trading as Taylor & Francis Group

Published online: 24 May 2024.

Submit your article to this journal

Article views: 203

View related articles

View Crossmark data

Full Terms & Conditions of access and use can be found at
https://www.tandfonline.com/action/journalInformation?journalCode=ysic20

STUDIES IN CONSERVATION
https://doi.org/10.1080/00393630.2024.2339711

ORIGINAL RESEARCH OR TREATMENT PAPER

OPEN ACCESS Check for updates

Mosaic Materials in an Art Deco Steel-framed Building

Grace A. Morris [1], Kevin Briggs [1], Michael Beare[2], Geoffrey Allen[3] and Richard J. Ball [1]

[1]Department of Architecture and Civil Engineering, University of Bath, Bath, UK; [2]CTP Consulting Engineers, Sevenoaks, Kent, UK; [3]University of Bristol, Bristol, UK

ABSTRACT

The mosaic coving at the Grade II* listed Freemasons' Hall in London is an example of a mosaic on an Art Deco steel-framed building. Microstructural and chemical characterisation of loose mortars and tesserae were undertaken to inform conservation efforts and advise whether a protective coating was needed to prevent further fading of gold gilding. Rigorous testing used optical imaging, scanning electron microscopy, field emission scanning electron microscopy, energy dispersive X-ray analysis, Raman spectroscopy, X-ray diffraction, and thermogravimetric analysis with differential scanning calorimetry. Laboratory evidence demonstrated the glass tesserae were created using traditional techniques. The glass tesserae were soda-lime-silica glass with lead. The gold glass tessera was produced in the ancient Roman style which included a glass *cartellina* layer, so further protective coating was not needed. Historical records confirmed sheets of mosaic tesserae were prefabricated in Italy. The grout and thin-set mortar were the same low hydraulicity mortar mix, which enabled mosaic tesserae positions to be adjusted as required. The bedding coat mortar was a hydraulic cement mortar that was applied on top of an early example of foamed mortar from 1932. This unique study analyses a traditional style mosaic that was installed during a pivotal point in construction history where foamed mortars and steel framed buildings were introduced. It demonstrates how archival research and laboratory testing of small-sized samples enhance the building's significance and architectural interest by improving the knowledge of its history.

ARTICLE HISTORY
Received November 2022
Accepted March 2024

KEYWORDS
Mosaic; lime mortar; scanning electron microscopy; energy dispersive X-ray analysis; Raman spectroscopy

Introduction

The Freemasons' Hall in London was built between 1927 and 1933 (Stubbs and Haunch 1983; The Library and Museum of Freemasonry 2006). The Grade II* building was designed by architects Henry Victor Ashley and F. Winton Newman (Historic England 1982). Inside, a vast mosaic coving was installed above the Grand Temple, which was designed by George Murray (Figure 1(a)) (Murray 1930; The buildings illustrated 1933). It was measured at approximately 16.5 m long on each side and 4 m tall. The combination of the mosaic coving and the early 1930s steel-frame construction have resulted in a splendid example of a mosaic in an Art Deco steel-framed building. Other prominent examples of mosaics in Art Deco steel-framed buildings include the head office at the Hong Kong and Shanghai Bank in Shanghai (1924) and Temple Emanu-El in New York (1930) (Singmaster 1998; Hart 2007). Mosaics built throughout the centuries have been known to fail due to moisture, for example at the Temple Emanu-El in New York and at the Basilica of San Marco (C11–C19) (Hart 2007; Allen et al. 2008; Dal Bianco and Russo 2012; Adami et al. 2018). Mosaics built from early C20 on steel-framed buildings face the additional threat of failure due to oxide jacking of embedded steelwork. This is what happened at the Freemasons' Hall mosaic, as evidenced in Figure 1(b,c).

The mosaic was formed using intricate arrays of different coloured small tesserae. Close inspection revealed cracks throughout the mosaic. The crack distribution was monitored by CAN London Ltd. They reported 65 cracks measuring between 0.21 m to 15.6 m long with crack widths between 0.25 mm to 7 mm (CAN London Ltd. 2012). The cracks were typically linear and occurred on all sides of the mosaic. The cracks ran through the grout and occasionally through the individual tesserae, as displayed in Figure 1(b). Cracks had loosened tesserae to the point that they fell away from the mosaic, as shown in Figure 1(d), onto the seating area below which was a safety risk. This initiated a coving repair project that aimed to ensure the structure was safe.

Visual deterioration was also occurring to some gold tesserae. The golden writing and other gold triangle edge features had lost their lustre over time whilst the golden rays, shown in Figure 1(d) had retained their lustre. It was considered desirable to either conserve

CONTACT Grace A. Morris gap37@bath.ac.uk Department of Architecture and Civil Engineering, University of Bath, Claverton Down, Bath, BA2 7AY, UK

© 2024 The Author(s). Published by Informa UK Limited, trading as Taylor & Francis Group
This is an Open Access article distributed under the terms of the Creative Commons Attribution License (http://creativecommons.org/licenses/by/4.0/), which permits unrestricted use, distribution, and reproduction in any medium, provided the original work is properly cited. The terms on which this article has been published allow the posting of the Accepted Manuscript in a repository by the author(s) or with their consent.

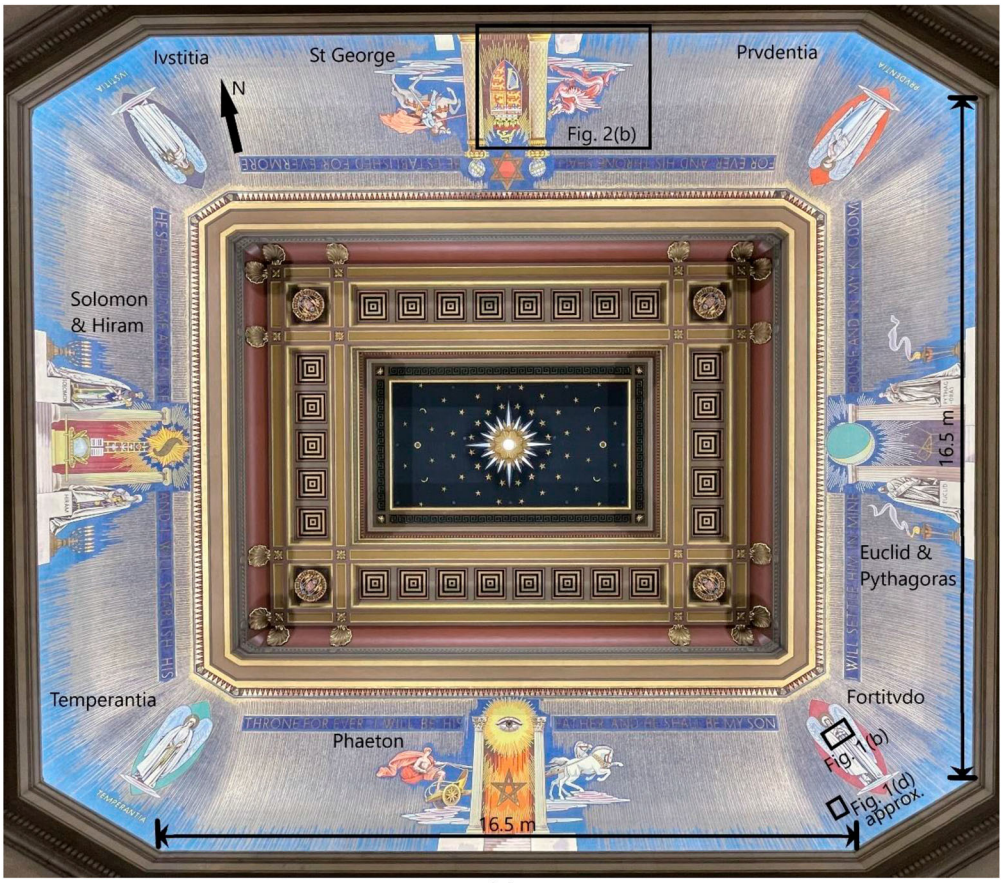

Figure 1. (a) The mosaic coving in the Grand Temple at Freemason's Hall; (b) Cracks through Fortitvdo are an example of the cracks scarring the mosaic; (c) Rust on the exposed steel structure in a crawl space to the skyward rear of the mosaic coving at the Freemasons' Hall; and (d) Gold and blue tesserae showing examples of spalled tesserae and the glass base exposed beneath the gold leaf.

the gold colour with a protecting coating over the mosaic or enhance the gold colour through regilding. Consequently, this study included investigating the gold tesserae and advising on whether a protective coating was beneficial to prevent further degradation.

This paper describes the material characterisation conducted before the coving repair. This study aimed to inform conservation works at Freemasons' Hall, to demonstrate how testing on limited sample sizes can reveal much about the materials and construction methods used, and to enhance the architectural interest of the building. Mortar and tesserae samples were analysed to understand how the mosaic was built, what materials were used, and whether the mosaic needed a protective coating to prevent further loss of surface gilding.

Background

There are three mosaic creation methods. First is the direct method where individual tessera are directly applied *in situ* to thin-set mortar. This thin-set layer should be tacky for adhesion but slow to set or carbonate so that adjustments can be made. The direct method is good for irregular surfaces but creates an undulating finish and requires workers to be on-site for the duration of the mosaic creation. Second is the indirect method where tesserae are adhered face down onto a backing sheet (Pugliese 2004). These pre-prepared sheets are then pressed onto a thin-set mortar and the backing is removed. The indirect method creates a flat finish, is easy to rework, and prefabrication reduces installation time. The third method is the double indirect method, which is like the indirect method except that tessera are stuck face up on the backing, prior to being transferred to a sticky backing on the top so that it can be applied to the substrate. Regardless of the method, the structure's surface must first be prepared with a bedding coat mortar before the thin-set mortar is applied. It was alleged that the Freemasons' Hall mosaic was installed by two Italians using the direct method, but historical evidence showed it was indirectly installed by three mosaic fixers (Museum of Freemasonry 2020).

George Murray designed the Freemasons' Hall mosaic (Clerk of Works 1932; The buildings illustrated 1933). His other mosaic works included the head office at the Hong Kong and Shanghai Bank in Shanghai which was also a steel framed building (The Evening Telegraph 1933; Singmaster 1998). Site diaries listed the mosaic fixer as 'Mr Avon of Venice' (Clerk of Works 1932; Cumbers 1932). This was possibly Gino Avon, who managed the workshop at the Fruili Mosaic School in the City of Spilimbergo until 1930, alongside his own workshop in the same city until 1934 when it was closed in compliance with the ruling fascist regime (Battiston and Grossutti 2019; Collendani n.d.). Mr Avon struggled to speak in English, so he was appointed two Italian speaking workers by Mr Stellon from the company Carter's (Clerk of Works 1932). This created a team of three Italian speaking mosaic fixers. Evidence of them using indirect method was in the Clerk of Works' diary which recorded that the mosaic shipment was delayed at Folkestone (Clerk of Works 1932). This was corroborated by the photograph in Figure 2(b) at locations (W) where two workers were applying mosaic sheets labelled with codes such as 'A75' (Sims 1932a). Using the indirect method and having two additional workers reduced the installation time. Documents stated the mosaic fixing started on 4 May 1932 and there was no mention of the fixing works after 22 June 1932, which gave an installation period of

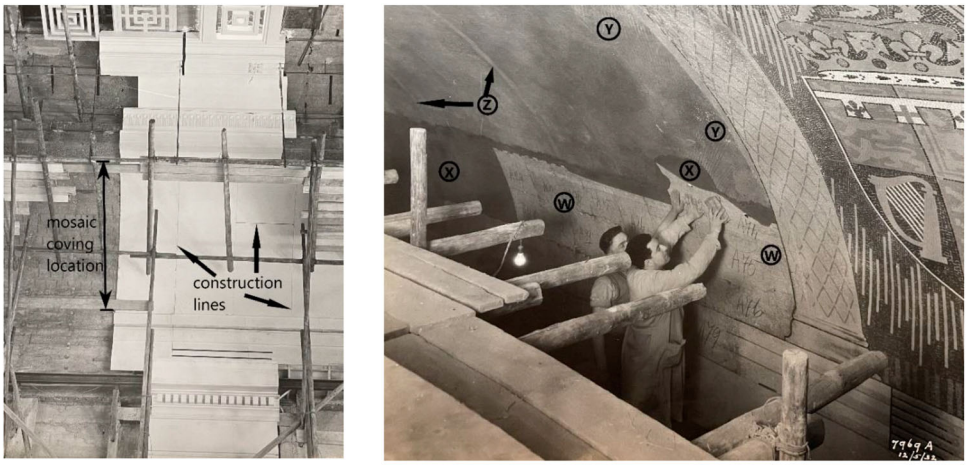

(a) (b)

Figure 2. Historical photographic records of (a) the site construction mock-up of the Grand Temple ceiling taken on 24 July 1931 © Museum of Freemasonry, London; and (b) two craftsmen installing prefabricated mosaic sheets for St George taken on 12 May 1932 © Museum of Freemasonry, London (Sims 1931; 1932a).

approximately seven weeks (Clerk of Works 1932; Cumbers 1932).

Initial visual inspection of the mosaic showed a composite structure with four layers on top of the building's structural concrete. The tesserae were at the front of the mosaic and were 5–7 mm thick. Gaps between tesserae were filled with grout and the tesserae were bedded onto a 1–2 mm-thick thin-set mortar. The thin-set mortar, which is visible at locations (X) in Figure 2(b), was applied to a bedding coat. Locations (Y) in Figure 2(b) show the scratched bedding coat, which was approximately 20 mm thick (Sims 1932a). Below the bedding coat there was a 12 mm-thick cementitious layer that was likely foamed mortar cast to create the desired curvature as seen in the construction mock-up in Figure 2(a) (Sims 1931). Foamed mortar is a high porosity cementitious slurry with no large aggregate that can be pumped and cast *in situ*. Location (Z) in Figure 2(b) shows construction lines demarking edges of cast foamed mortar sections. Finally, behind the foamed mortar was a structural concrete that encased the building's steel frame, as seen in Figure 1(c).

Two 10 mm holes were drilled by Format NDT Ltd to facilitate ultrasonic surveying of defects using a Mitec mfd650c and video inspection with an Aadark 8802AL inspection camera. The total depth was 200–220 mm in the two video surveyed locations and no void spaces were identified in these locations (Format NDT LTD 2018). The mosaic build up was approximately 40 mm in total from the tesserae to the back of the foamed mortar, though material thicknesses varied. The remaining 160–180 mm of the depth was the structural concrete.

Methods and materials

Sample collection from site was limited to loose mortar and glass tesserae, so pieces of structural concrete and tesserae of every colour could not be obtained. Mortar samples were extracted from each of the four identified surface layers: 'grout', 'thin-set mortar', 'bedding coat', and 'foamed mortar'. Drilling for ultrasonic testing and video inspection created a by-product 'powder' which contained small amounts of the 'thin-set mortar', 'grout', 'bedding coat', and 'foamed mortar' alongside the structural concrete. The powder was analysed to check for any carbon-based materials, such as hessian, used in the mosaic build up and to check for anything atypical in the structural concrete.

There were a range of coloured glass and ceramic tesserae, but only three glass tesserae were acquired: one gold glass tessera and two blueish turquoise glass tesserae (referred to as 'blue'). The extracted tesserae specimens were approximately square, measuring 12 ± 1 mm wide in both directions, 4.9 ± 0.1 mm deep for the 'blue' tessera, and 6.5 ± 0.1 mm deep for the 'gold' tessera. All tests to tesserae were to be non-destructive so that tesserae could be reinstated. This limited the tesserae testing to imaging using optical microscopy and scanning electron microscopy (SEM), and characterisation using energy dispersive X-ray analysis (EDX) and Raman spectroscopy.

For optical microscopy a Keyence VHX 6000 equipped with the VH-Z20R/Z20 T lens was used, enabling magnifications between ×20 and ×200. SEM imaging with backscatter electron imaging was carried out using a JEOL SEM6480LV. EDX was carried out on the fracture surfaces of uncoated samples using the JEOL SEM6480LV equipped with an Oxford INCA X-Act SDD X-ray detector. A Renishaw inVia system was employed to carry out the Raman spectroscopy and Renishaw WiRe 4.0 software enabled peak fitting of the spectra. Samples were examined using a monochromatic 532 nm or 785 nm wavelength laser to allow the spectrum to be obtained and avoid excessive fluorescence.

For mortar samples, laboratory testing included optical microscopy imaging of polished samples, SEM and field-emission scanning electron microscope (FE-SEM) imaging of fracture surfaces and polished samples, and characterisation using EDX, X-ray diffraction (XRD) analysis, thermogravimetric analysis (TGA) with differential scanning calorimetry (DSC), and Raman spectroscopy.

The FE-SEM used was a JEOL JSM-7900F. XRD was carried out using a BRUKER AXS D8 Advance, equipped with a Vantec-1 detector, using CuK_{α} radiation. For XRD analysis the grout sample was flat, so it was mounted, but the other mortar samples were ground to powder. The software WinXPOW was used for phase identification of the results. For TGA and DSC, samples were placed in an alumina crucible for use in the Netzsch STA 449 F1 Jupiter simultaneous thermal analyser. The temperature was increased from 30°C to 900°C at a rate of 10°C per minute. Data were recorded and processed using the Netzsch Proteus software.

SEM imaging was conducted on fracture surfaces and polished mortar samples for inspection of sample morphology, microstructure, and the distribution of aggregate, binder, and pores. Fracture surfaces of mortar samples were sputter coated with gold (Au). FE-SEM was carried out on a polished and fracture sample of the foamed mortar, which enabled greater magnifications for observation of particle morphology.

Calcium carbonate crystallises as calcite, aragonite, or vaterite. Calcite is typically observed in its rhombohedral form but may be present in its tabular, prismatic, acute rhombohedron, or scalenohedral habit (Cizer et al. 2012; Serrapede et al. 2014). Aragonite crystals are acicular whilst vaterite crystals are typically spherical but are occasionally star shaped if irregular growth occurs (Zhou et al. 2004; Serrapede et al.

2014; Trushina, Bukreeva, and Antipina 2016). In the case of samples with incomplete carbonation, calcium hydroxide is characterised by plate-like hexagonal crystals (Rodriguez-Navarro, Hansen, and Ginell 1998; Pesce et al. 2017). In hydraulic pastes dicalcium silicate (C_2S) and tricalcium silicate (C_3S) hydrate in the presence of water, producing calcium-silicate-hydrate (C–S–H) phases. These are needle-like in shape and as hydration continues the C–S–H layer grows in thickness, the fibres interlock, and the C–S–H gel layer increases in density (Mindess and Francis Young 1981). Gypsum is incorporated into cement to prevent the 'flash set' caused by hydration of tricalcium aluminates (C_3A) in the binder. C_3A reacts with gypsum to produce a mineral that is colloquially called 'ettringite' (AFt) (Bullard et al. 2011). Ettringite crystals are acicular and hexagonal in cross-section. Once the calcium sulphate is consumed, remaining C_3A reacts with ettringite to produce calcium monosulphoaluminate (AFm) which are hexagonal plate-like particles (Yoneyama et al. 2021).

EDX of the mortar samples reveals the chemical composition of the analysed area. For mortar samples the elemental weights identified in the binders were converted to oxides and input into Equation (1) which calculated the cementation index (CI) (Holmes and Wingate 1997, 13). Equation (1) used element weights to estimate the binder's hydraulicity. The bottom of the fraction added quicklime (CaO) and magnesium oxide (MgO). The top of the fraction summed silica (SiO_2), alumina (Al_2O_3), and haematite (Fe_2O_3). These were the active clay contents in the binder that create hydraulic phases. Ideally the CI would be calculated from fresh binders and oxide analysis would be carried out using X-ray fluorescence. In this case samples contained aggregate and equipment availability restricted testing to chemical analysis by EDX. The visible aggregate was sieved out of samples with a 63 µm sieve before EDX, but fine-grained quartz remained in the mortar which skewed the CI results towards more hydraulic classifications. As such, the results did not accurately describe the hydraulicity but offered an approximation of the hydraulicity and enabled comparison of hydraulicity between mixes.

$$CI = \frac{2.8SiO_2 + 1.1Al_2O_3 + 0.7Fe_2O_3}{CaO + 1.4MgO} \quad (1)$$

Results

Optical microscopy images of the blue and gold tesserae are shown in Figure 3(a–d). Measurements demonstrated that these tesserae were hand-cut with vertices ranging from 85° to 98° in the blue tessera and 87° to 92° in the gold tessera. The top surface of the blue tessera in Figure 3(a) had surface imperfections where dirt had accumulated but there were no cracks. Viewing the blue tessera on its side in Figure 3(b) revealed a homogeneous opaque blue glass. There were grout remnants adhered to the side and contained in partial bubble voids that remained from glass production and were indicative of poured glass.

Optical microscopy confirmed that the gold tesserae were created using an ancient Roman method where gold leaf foil was sandwiched between support glass and a thin glass layer called the *cartellina*. The exact order of this process can vary (Neri and Verità 2013). The gold leaf seen in Figure 3(c) was covered by a transparent *cartellina*. The *cartellina* was the 0.5 mm-thick top layer in Figure 3(d). No bubbles were identified in the *cartellina* and it had a wavey surface profile which signified blown glass. The support glass beneath the gold leaf had a greenish hue and had a flat bottom face except for occasional chipped areas. It also had an abundance of bubbles which meant the support glass was made using poured glass.

Microcracks were found in the *cartellina* in Figure 3(c) and in the top third of the support glass. These cracks were likely the result of thermal expansion and shrinkage during the gold glass production. The presence of these microcracks in the *cartellina* and in the adjacent topmost portion of the support glass demonstrated that the blown glass *cartellina* was made first. This was confirmed by the exposed support glass on some tesserae, which was visible in Figure 1(d). Here the poured support glass had flowed over the edge of the *cartellina*, leading to visible support glass when tesserae were cut from the edge (Neri and Verità 2013).

Imaging during EDX analysis of the blue tesserae showed that the glass was one smooth piece with some adhered surface particles up to 5 µm and frequent features up to 8 µm wide. These can be seen in Figure 4(a). The SEM image in Figure 4(b) shows the ancient Roman style of gold leaf glass with the gold leaf foil between the *cartellina* (left side of the image) and the support glass (right side of the image). The gold leaf was visually evident and had been beaten to less than 0.5 µm thick.

EDX spectra were obtained for each sample using one or more sites of interest. Table 1 presents weighted averages over the total area analysed for each material. EDX analysis of the top and side of the blue glass tessera revealed it was composed elementally from carbon (C), oxygen (O), sodium (Na), magnesium (Mg), aluminium (Al), sillcon (Si), potassium (K), calcium (Ca), copper (Cu), lead (Pb), and antimony (Sb). The glass on base of the gold tesserae had a similar composition to the blue tessera but with a higher proportion of aluminium and only trace amounts of copper. The gold leaf identified in Figure 4(b) was analysed and

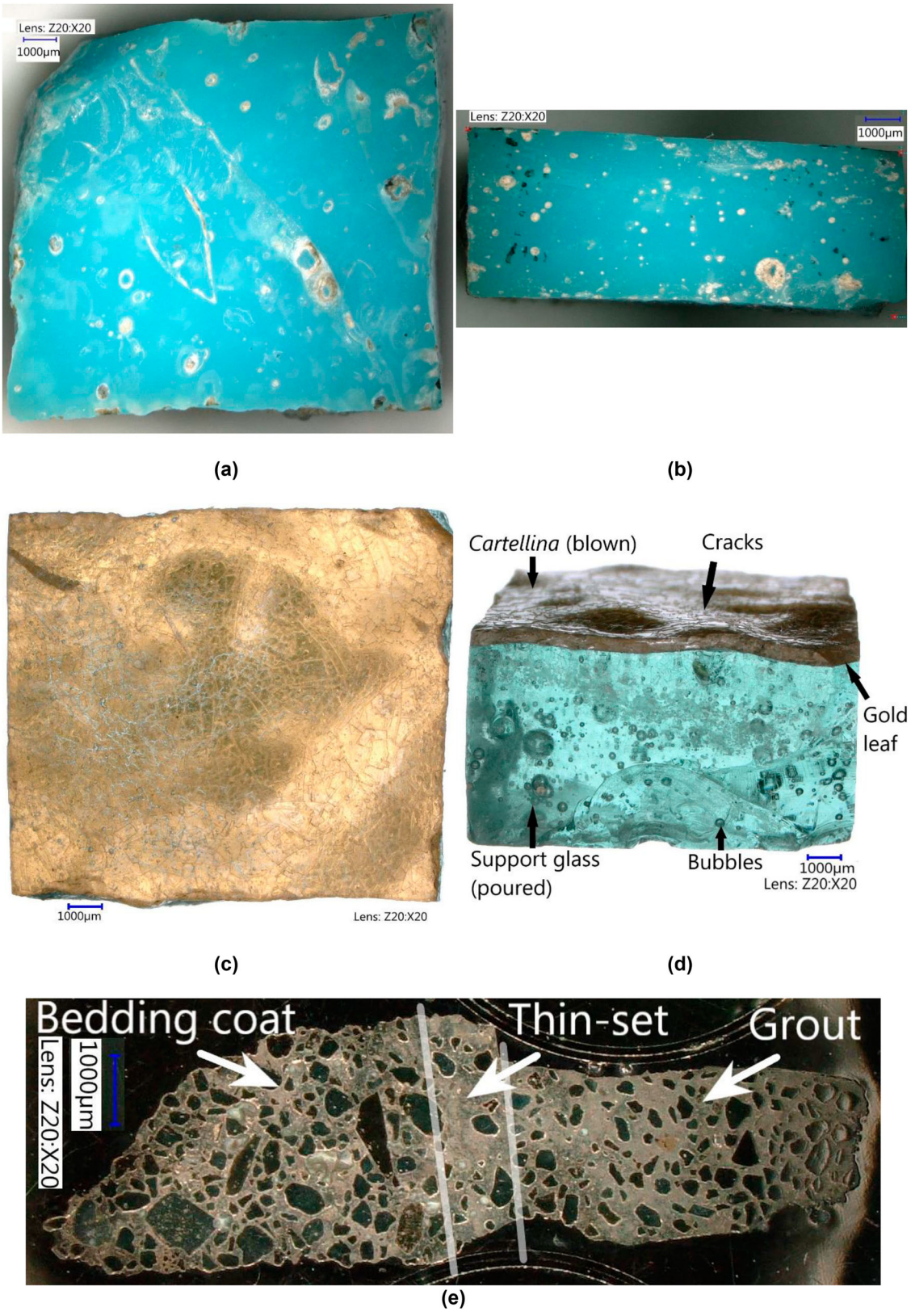

Figure 3. Optical microscope images of (a) a blue tessera taken at ×20 magnification from the top; (b) the same blue tessera from the side at ×20 magnification; (c) the top surface of the gold tessera showing the gold leaf through the cartellina taken at ×20 magnification; (d) a side view of the same gold tessera; and (e) a polished section through the intermediate grout, thin-set mortar, and bedding coat.

confirmed to be gold (Au). No gold alloying elements were identified, confirming 24-carat gold was used for the gold leaf. The *cartellina* contained 0.5% manganese (Mn). The blue tesserae and the glass either side of the gold leaf layer contained impurities including iron (Fe) and chlorine (Cl).

The Raman spectrum of the blue tessera in Figure 5 had an initial peak that was the Boson peak. The Boson

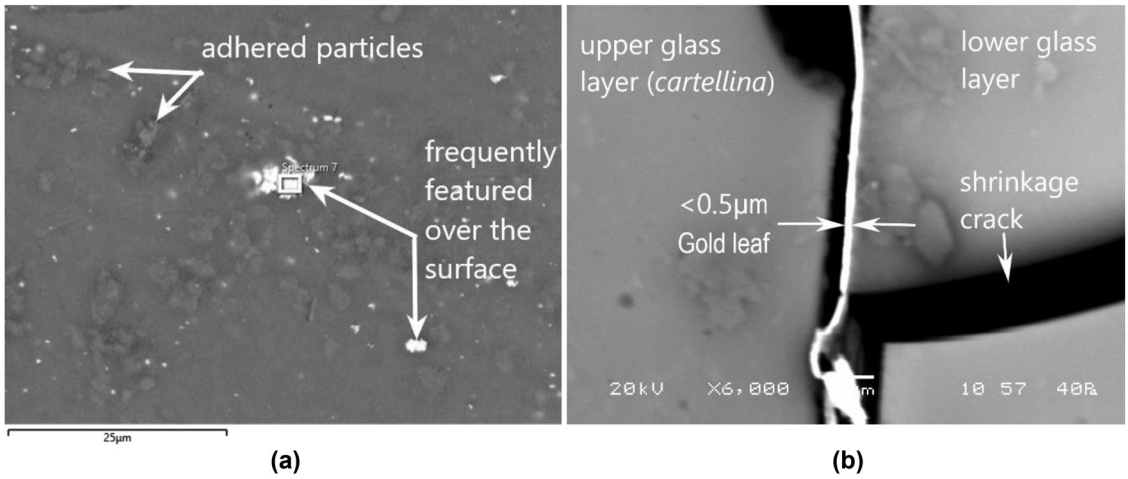

Figure 4. (a) Backscattered electron image of the side of the blue tessera taken during EDX analysis; and (b) SEM image of the side of the gold tessera at ×6k.

Table 1. Elemental analysis by EDX for mosaic mortar and tesserae samples.

Material	Area analysed (μm²)	Element weight averaged over EDX results (%)															
		C	O	Na	Mg	Al	Si	K	Ca	Cu	Au	Pb	S	Mn	Fe	Cl	Ti	Sb
Powder	32,500	6.3	39.4			1.4	27.8	0.7	19.8				0.7		4.1			
Foamed mortar	16,200	3.6	39.6	4.8		10.9	26.8	5.2	6.3					0.6	2.2	0.3		
Bedding coat	38,300	5.6	40.5	0.8	0.3	3.3	13.1	1.6	29.6				3.1		1.7		0.2	
Thin-set	2440	4.5	33.8	0.2	0.3	2.1	7.2	0.4	49.7				0.6		1.2			
Grout	14,400	3.2	37.3			1.3	4.4	0.3	52.2				0.9		0.5			
Blue tessera top	13,100	3.0	33.2	5.9	0.3	0.3	31.1	0.6	5.9	1.7		17.1	0.7			0.1		
Blue tessera side	22,500	10.0	42.5	4.2	0.3	0.2	25.6	0.5	3.9	1.0		10.6			0.1			1.0
Gold tessera Base	265,000	3.2	31.2	1.3	0.3	1.4	34.8	1.2	3.7			22.9						
Gold leaf	65	5.7	18.1	1.8	0.1	0.7	12.0	0.6	1.7	0.2	49.5	8.3	1.2	0.1		0.1		
Gold tessera *Cartellina*	145,000	3.4	32.3	1.4	0.2	1.8	36.7	0.9	3.8			18.9		0.5		0.1		

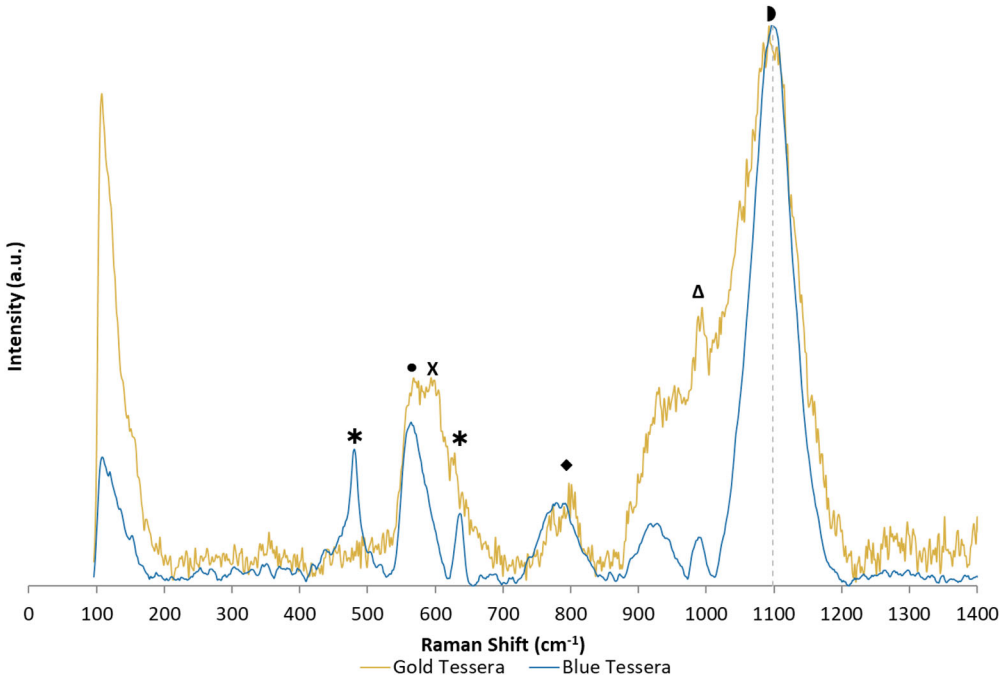

Figure 5. Raman spectra for the gold tessera and a blue tessera. '✱' – Calcium antimonate ($Ca_2Sb_2O_7$), '●' – symmetric stretching of Si–O–Si in mode Q_3, 'X' – symmetric stretching of Si–O–Si in mode Q_2, '◆' – stretching of Si–O in SiO_4 cage, 'Δ' – stretching of Si–O in mode Q_2, '◗' – stretching of Si–O in mode Q_3.

peak is a feature characteristic of amorphous materials that results from excess vibrational density of states. In glasses the Boson peak is a broad peak between 20 and 150 cm^{-1} (Schroeder et al. 2004; Deschamps et al. 2011). The blue tessera also contained peaks of calcium antimonate at 480 and 636 cm^{-1}. It was present in the orthorhombic form ($Ca_2Sb_2O_7$) as opposed to the hexagonal crystal ($CaSb_2O_6$) (Gedzevičiute et al. 2009; Ricciardi et al. 2009; Zhao et al. 2013). Both the gold and blue Raman spectra exhibited peaks corresponding to stretching vibration modes of sillcon and oxygen in the lead glass. The band at 564 cm^{-1} was attributed to Si–O–Si symmetric stretching vibration mode Q_3, the band at 792 cm^{-1} was Si–O stretching in its tetrahedral oxygen cage (SiO_4), and the 988 and 1098 cm^{-1} bands were Si–O stretching in vibration modes Q_2 and Q_3, respectively (Deschamps et al. 2011).

Optical microscopy was used to calculate the aggregate contents for the mortars in the polished section in Figure 3(e). The percentage of aggregate by area was 17.3% for the grout, 10.3% for the thin-set, and 30.5% for the render. This demonstrated that the render mix design had a greater proportion of aggregate in the mix design compared to the grout and thin-set mortar. Aggregate percentage could not be carried out on the foamed mortar due to the absence of any visible aggregate.

SEM imaging of the mortars revealed calcite crystals in the grout and thin-set mortar, as shown in Figure 6(a), with no evidence hydraulic phases. This implied that a high calcium lime mortar had been used. Ettringite crystals over 10 µm in length and C–S–H fibres were identified in the SEM image of the bedding coat mortar in Figure 6(b), meaning that the bedding coat had hydraulic properties and that there was sulphate present in the mortar. There were no distinguishable crystals or fibres in the foamed mortar in Figure 6(c) due to compaction, no aggregate was visible, and there was a significant proportion of void space. At this magnification (×2000) the largest visible pores were over 20 µm in diameter, indicating a low density, porous mortar. Further imaging of these pores showed that they were well connected, however the sample was too small to run a mercury intrusion porosimetry test so the pore size distribution could not be obtained. The interface between the foamed mortar and bedding coat layer was clearly visible in Figure 6(d) as a smooth line between the two mortars. The image accentuated the difference in their structure and composition. Aggregate was clearly seen in the bedding coat mortar, surrounded by binder, and containing occasional void spaces. The foamed mortar structure had no distinguishable aggregate and was extremely porous with the largest visible pore measuring 175 µm in diameter at ×100 magnification. The foamed mortar's pores were partially filled at the interface.

Field-emission scanning electron microscopy (FE-SEM) of the foamed mortar revealed aragonite and calcite in Figure 6(e) and (f), respectively. The surfaces of the pores were covered in spherical particles of around 100 nm in size, which was consistent with silica fume in Khan et al. (2014) and Esfandiari and Loghmani (2019). Occasional fibrous hydration products were present, as in Figure 6(h) (Tantawy et al. 2012).

EDX results in Table 1 showed that the thin-set and grout samples had similar elemental composition. The main elements identified in the thin-set and grout were calcium and sillcon with some aluminium and iron. This composition indicated that a calcium rich lime with a small amount of hydraulicity had been used for both the grout and thin-set mortar. Bedding coat samples showed a higher proportion of sillcon, iron, and aluminium compared to the thin-set and grout. Sulphur also appeared in the bedding coat layer. The bedding coat elemental composition denoted a mortar with hydraulic properties. The foamed mortar had significantly less calcium by weight than the other mortars and a greater proportion of aluminium and potassium. It also had more iron by weight than the other mortars but less than in the drilling powder. The EDX results for the foamed mortar were consistent with a cementitious material (Scrivener et al. 2016). The powder sample contained and represented all the mortars. Iron was identified in higher proportions in the powder than in any of the mortar layers due to drilling through aggregate containing iron.

The CI results in Table 2 were calculated using Equation (1). The grout and thin-set mortar had CI of 0.77 and 0.45, respectively, whilst the bedding coat had a higher hydraulicity above the value of a natural cement. The foamed mortar CI was more than 14 times greater than the classification for natural cement owing to high concentrations of aluminium and sillcon and low calcium contents (Holmes and Wingate 1997). This showed that the foamed mortar was not a typical mix design.

The results obtained through Raman spectroscopy of the samples have been shown in Figure 7. The Raman spectra for the four mortar layers showed calcite bands at 154, 280, 714, and 1088 cm^{-1}. The grout was darker towards the mosaic surface where Raman spectroscopy revealed ettringite in the exposed surface grout at 988 cm^{-1} (Torréns-Martín et al. 2013). A number of unidentified peaks remained in the drilling powder >1070 cm^{-1}. It is thought that the higher wavelength bands could correspond to carbon containing material, but this could not be confirmed due to noise. Quartz was also identified in the drilling powder at 186, 206, and 455 cm^{-1} (Dean, Sherman, and Wilkinson 1982; Liu et al. 2015).

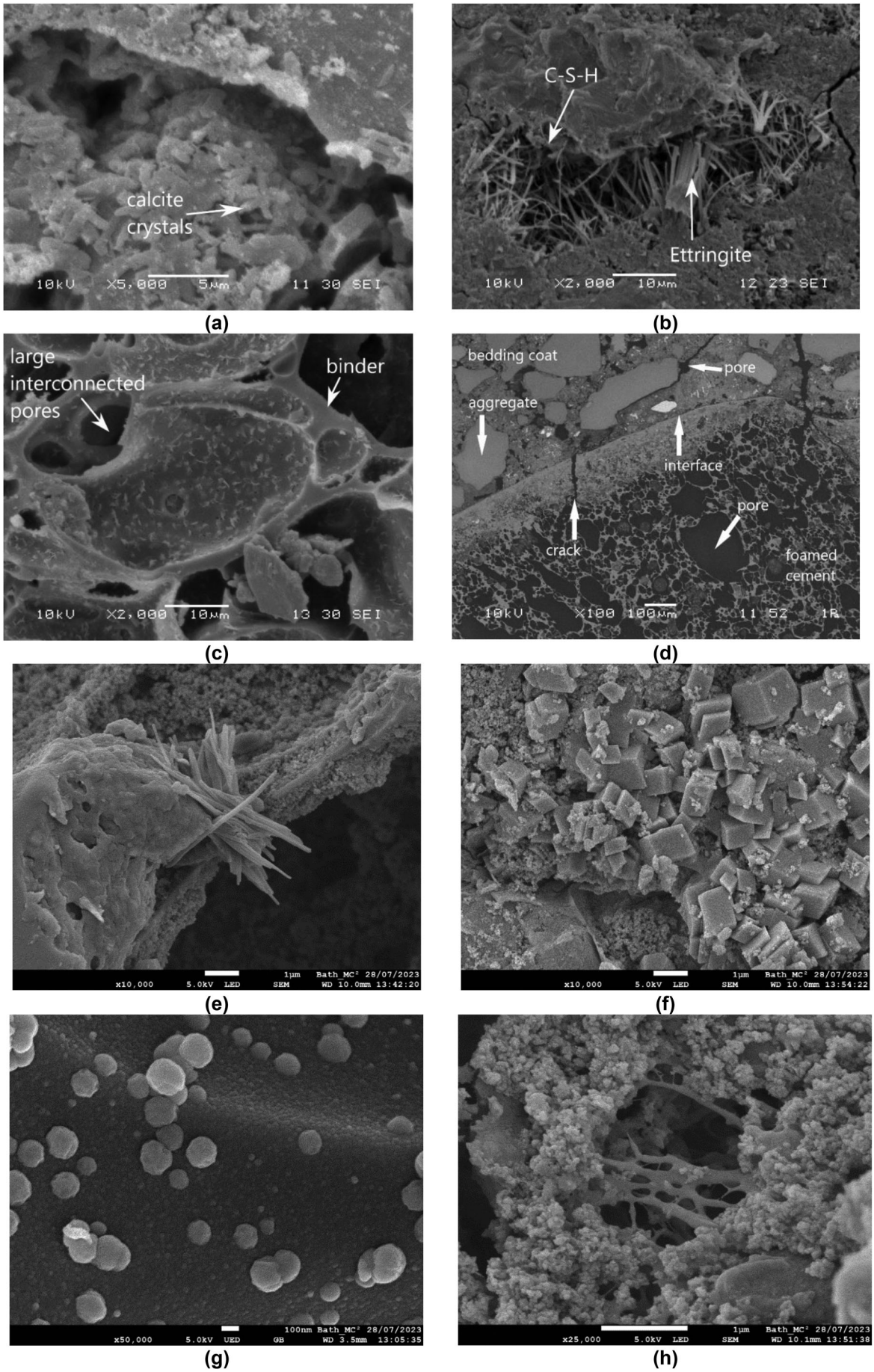

Figure 6. SEM images of the fracture surface of (a) the grout at ×5k; (b) the bedding coat mortar at ×2k; (c) the foamed mortar substrate at ×2k; and (d) the bedding coat and foamed mortar interface at ×100. FE-SEM images from the foamed mortar of (e) aragonite at ×10k; (f) calcite at x10k; (g) silica fume at ×50k; and (h) fibrous hydration products at ×25k.

Table 2. Classification of hydraulicity for the tested lime binders based on cementation index classification (Holmes and Wingate 1997).

Classification	CI
Fat lime	Close to zero
Mildly hydraulic	0.3–0.5
Moderately hydraulic	0.5–0.7
Eminently hydraulic	0.7–1.1
Natural cement	1.7

Binder	CI	Classification
Foamed mortar	23.85	N/A
Bedding coat	2.8	Natural cement
Thin-set mortar	0.45	Mildly hydraulic
Grout	0.77	Eminently hydraulic

XRD results for the four mortars are presented in Figure 8. The XRD results for the grout corresponded with the results for the thin-set mortar. In the grout and thin-set mortar the calcite and quartz bands had the highest intensities with some less intense peaks corresponding to portlandite and hydrated silicates. The presence of the portlandite meant that carbonation had been inhibited in areas in the grout. The hydrated silicate peaks confirmed that the grout and thin-set mortar had hydraulic phases present. Only calcite and quartz were identified in the bedding coat. The foamed mortar was found to contain no quartz but had calcite, calcium alumina silicate hydrate (C–A–S–H), and vaterite which is the most thermodynamically unstable polymorph of calcite (Wehrmeister et al. 2010). XRD confirmed that the foamed mortar had hydraulic properties but contained no quartz aggregate.

TGA and DSC results for the drilling powder, which contained samples from all the mosaic mortar layers and the structural concrete, are presented in Figure 9 as an example of the TGA, derivative thermogravimetry (DTG), and DSC data obtained. For all samples the abundance of each identified compound has been summarised in Table 3. In all samples mass loss taking place up to 100°C corresponded to water evaporation. Dehydroxylation of portlandite occurred at 475°C in the thin-set, grout, and the drilling powder. The mass loss of H_2O was used to back-calculate portlandite contents. Portlandite was calculated as 4.11 times the percentage mass loss over the temperature range for dehydroxylation of portlandite. Portlandite contents were low but demonstrated that even after 90 years the grout, thin-set, and structural concrete had not fully carbonated. This was due to impermeable tesserae restricting carbonation rates. In all mortars, significant mass loss occurred around 700–800°C where calcite decarboxylation calcite took place. The mass percentage of calcite was calculated as 2.27 times the percentage mass loss due to decarboxylation. The grout and thin-set mortar contained the greatest proportions of calcite. Peaks were present at 145°C in samples containing the bedding coat or foamed mortar which was in the region of dehydration of gypsum, C–A–H, and C–S–H but the characteristic double peaks of gypsum were not present in any sample (Lawrence et al. 2006;

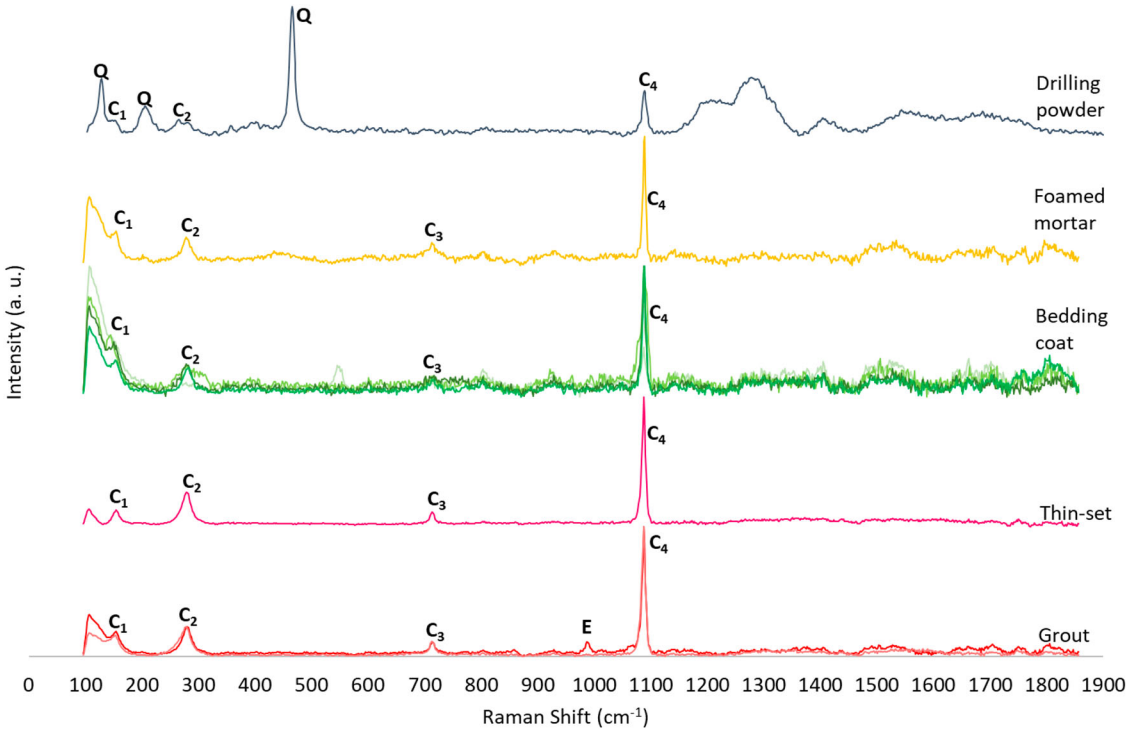

Figure 7. Raman spectra for mosaic mortars showing identified vibrational peaks. 'Q' – symmetrical stretching in quartz; 'C_1' – translation of CO_3^{2-} in calcite; 'C_2' – rotational torsion of C–O in calcite; 'C_3' – in-plane deformation of C–O–C in calcite; 'C_4' – symmetric stretching of C–O in calcite; and 'E' – v_1 symmetric stretching of SO_4^{2-} in ettringite.

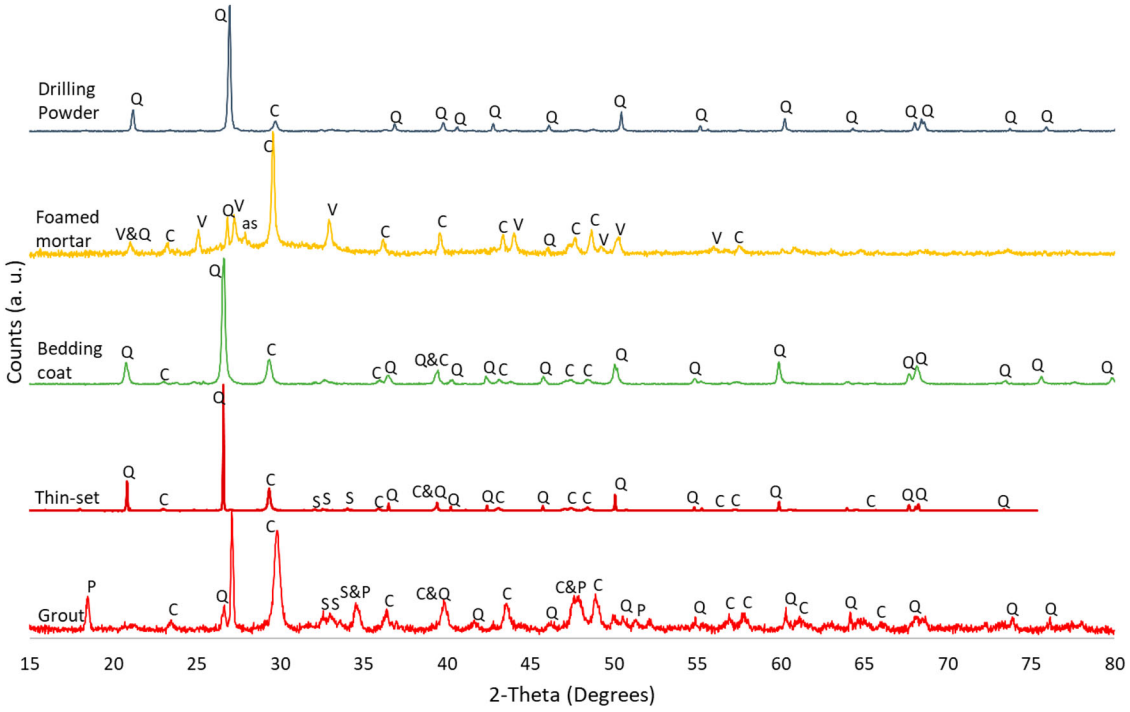

Figure 8. XRD results for the grout, thin-set mortar, bedding coat, foamed mortar, and drilling powder. 'C' – calcite; 'P' – portlandite; 'S' – hydrated silicates; 'Q' – quartz, 'V' – vaterite; and 'as' – calcium alumina silicate hydrate (C–A–S–H).

Lothenbach, Durdziński, and de Weerdt 2016). There was a subtle peak in the bedding coat and drilling powder at 250–300°C which was attributed to goethite, an iron oxide impurity in the sand (Lawrence et al. 2006). This confirmed that aggregate impurities caused the elevated iron in the drilling powder EDX results. The peak identified in the DSC plots at 580°C corresponded to quartz inversion where it transitions from α-quartz to β-quartz (Netzsch 2008; Arcones-Pascual, Hernández-Olivares, and Sepulcre-Aguilar 2016). All samples exhibited the quartz transition peak except for the foamed mortar, further demonstrating that there was no quartz aggregate in the foamed mortar.

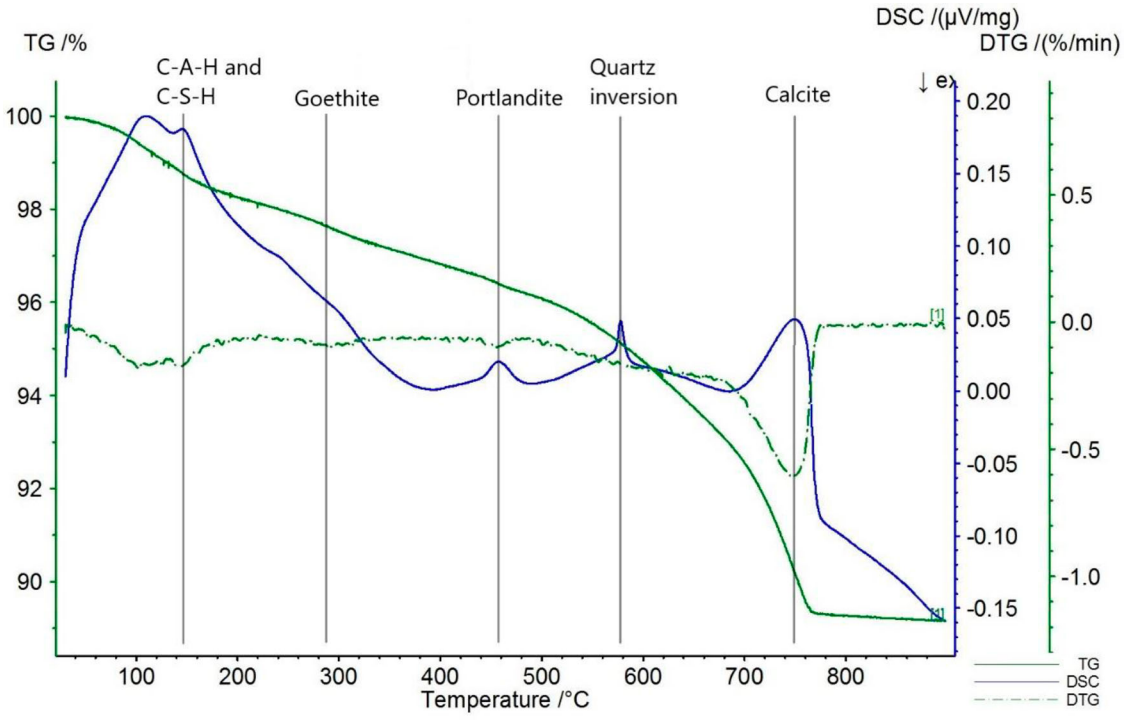

Figure 9. TGA/DSC results for the drilling powder obtained after drilling which includes the grout, thin-set mortar, bedding coat, and foamed mortar.

Table 3. Abundance of compounds identified by TGA and DSC.

Sample	C–-A–H and C–S–H	Goethite	Portlandite (%)	Quartz inversion	Calcite (%)
Drilling powder	+	+	++ (1.23)	++	+++ (8.09)
Foamed mortar	++	-	-	-	+++ (10.35)
Bedding coat	+	+	-	++	+++ (7.69)
Grout, thin-set and bedding coat	+	-	++ (1.56)	++	+++ (12.01)
Thin-set	-	-	++ (1.27)	++	+++ (16.44)
Grout	-	-	-	++	+++ (13.79)

Note: - not identified, + sparse, ++ common, +++ abundant.

Discussion

The mosaic was handmade using hand-cut tesserae produced in Italy at a time when the Fascist regime limited art exports. The composition of the handmade glass tesserae varied depending on the colour and optical properties required. The chemical elements identified by EDX arose from various compounds that were added by the craftsmen to achieve optimal working and visual properties. The compounds identified in the tesserae and their use in glass have been summarised in Table 4.

EDX results show that both colours of glass tesserae used soda-lime silica glass with lead oxide introduced to enhance the optical properties. Sodium oxide was used in the soda-silica glass tesserae as a flux to lower the glass' melting temperature from 1713°C to below 1000°C (Brill 1963; Jones 1971; Rasmussen 2012). Soda-silica glass is soluble in water, so lime was added to stabilise the glass by increasing its durability and chemical stability. A portion of the lime stabiliser may have been dolomitic lime which would account for the presence of magnesium in the glass, but this could not be confirmed. The iron and aluminium were present due to impurities in the sand (Boschetti et al. 2016).

Different compounds were added to the glass mix to achieve a clear *cartellina* and the blue opaque glass. The *cartellina* glass in the gold tessera had a manganese-based decolourant to counteract the colouring effects of impurities present and improve the visual impact of the gold leaf through the *cartellina*. This decolourant was unique to the gold tessera *cartellina* and was not present in the support glass or in either of the blue tesserae tested. The gold tessera's support glass was embedded so a decolourant was not required. The colour in the blue glass tessera was achieved using copper oxide and the opacifying agent was the orthorhombic form of calcium antimonate ($Ca_2Sb_2O_7$).

Table 4. Compounds identified in gold and blue tesserae and the properties achieved.

Compound	Use
Sodium oxide	A flux that lowered glass temperature from 1713°C to below 1000°C.
Sillcon dioxide	Fundamental constituent of glass.
Calcium oxide	Lime stabilised the soda-silica glass.
Magnesium oxide	Magnesium oxide indicated that dolomitic lime may have been used as the stabiliser.
Lead oxide	Added to improve the refractive index and as a flux. Lead glass is colloquially termed 'crystal'.
Copper oxide	Introduced the blue-green colour of the blue tesserae.
Potassium oxide	Used to slow crystal growth and reduce the temperature of the upper limit of crystallisation by up to 50°C, increasing workability and quality.
Calcium antimonate	Opacifying agent or white colour.
Manganese dioxide	Decolourant.
Gold	24-carat gold leaf was sandwiched between to glass layers to create gold tesserae.

The technique for creating the ancient Roman gold leaf glass was inferred from visual inspection and optical microscopy. Production began with a thin *cartellina* layer made from blown glass. The gold leaf was then applied, then this *cartellina* and gold leaf composite was reheated so that the molten support glass could be poured on. Finally, the three layers were compressed to ensure good contact (Neri and Verità 2013). As a result of this compression, the molten poured support glass took on the form of the flattening tool which created the straight edge at the base of the tessera in Figure 3(d).

As part of the conservation work it was questioned whether the mosaic needed a protective coating to prevent further loss of the gold lustre. Analysis of the gold glass tesserae revealed the gold leaf was protected by a *cartellina*, which explained why the gold tesserae in the rays in Figure 1(d) had retained their colour and confirmed that gold glass tesserae did not need additional protective coating. However, inspection of George Murray's mosaic design and a photograph taken during installation revealed the fading writing and triangle features were originally not gilded, so they were not made using ancient Roman style gold leaf glass (Murray 1930; Sims 1932b). These elements were surface gilded later, with the gilding application potentially shown in a 1935 photograph (Anon 1935). A protective coating would preserve the existing shade of the exposed gilding, but a coating over the mosaic was inadvisable because the other coloured tesserae and glass tesserae do not need it. Moreover, it would restrict moisture transfer through the grout and promote moisture accumulation inside the mosaic, generating associated moisture induced decay. Instead, fading gold ceramic tesserae were regilded.

A summary of the mosaic build-up is presented in Figure 10, including information on the mortar mixes

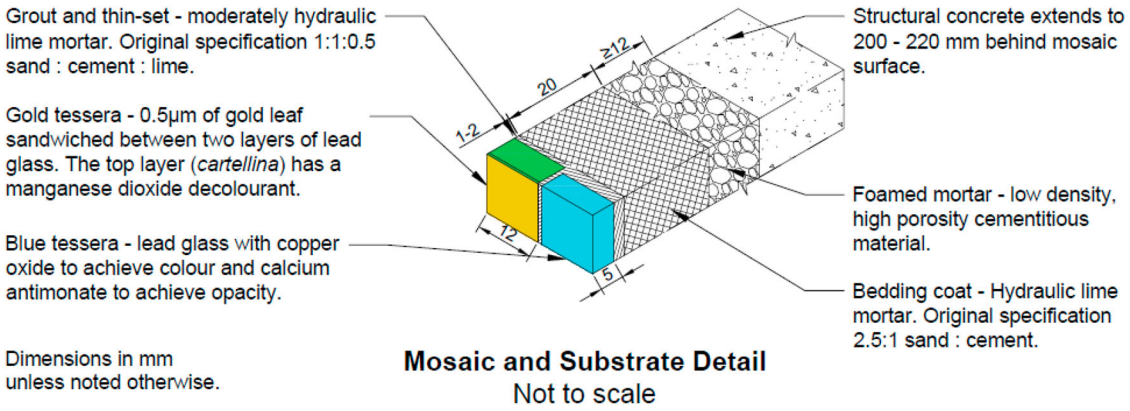

Figure 10. Diagrammatic representation of the mosaic build-up.

used and their location with respect to the tesserae. The thin-set and grout layers both had evidence of calcite crystals in SEM images, similar EDX compositions, and similar Raman and XRD spectra. Raman spectroscopy revealed that the mosaic surface has been exposed to sulphates over its lifetime, leading to ettringite formation in the top-most portion of the grout. XRD spectra revealed calcite and quartz with some portlandite and hydraulic phases. TGA/DSC confirmed calcite with small amounts of portlandite remaining in the thin-set layer. For the grout and thin-set mortar the impurities identified in the EDX indicated a low hydraulicity lime binder was used with quartz aggregate. These results showed that the same lime mortar mix design was used beneath (thin-set layer) and around (grout) the tesserae. Optical imaging showed a low proportion of aggregate compared with the bedding coat. This low hydraulicity lime mortar would have been tacky with a relatively long working time. This neither evidences the indirect nor the direct method so historical records and visual inspection remained integral for determining the installation method. Historical records confirmed that the indirect method was used for fixing the mosaic (Clerk of Works 1932; Sims 1932a). The records also contained only two mortar specifications for the thin-set and the render, confirming that the thin-set and grout were the same mix design. The thin-set specification was 1:1:½ of sand to cement to lime (Clerk of Works 1932). This is consistent with the results obtained for the grout and thin-set.

SEM imaging of the bedding coat revealed both C–S–H fibres that are associated with hydraulic mortars and EDX results showed a higher proportion of sillcon and aluminium compared to the thin-set and grout. These results showed that the bedding coat was a mix of quartz aggregate and a hydraulic binder. Historic records supported the laboratory results by stating that the bedding coat was specified 2½:1 sharp sand to cement (Clerk of Works 1932).

SEM of the foamed mortar showed it was significantly porous and it was indicative of a low-density material. This low-density mortar may have been specified for ease of construction and to reduce the structure's weight. Figure 2(a) shows boarding in the construction mock-up, and construction lines are visible in Figure 2(b). These construction lines demarked the boarding positions from when the foamed mortar was cast. The foam mortar created a smoother, lightweight layer that was cast to achieve the desired form. It is possible that the observed cracks coincided with the joins between these boards, but it could not be confirmed without intrusive surveys. The pore sizes identified in SEM images were typical of air-entrained concrete (Silva et al. 2020). The EDX results, and the size and abundance of pores, indicate foamed mortar. The earliest known patent for foamed mortar was filed in 1923 and casting at the Freemasons' Hall took place in 1932, so this represented a relatively early use of foamed mortar in construction (Eriksson 1924). Historical records state that 'aerocrete', which is an alternative name for foamed mortar, was used elsewhere in the Freemasons' Hall (Clerk of Works 1932). This shows that the contractors were familiar with using 'aerocrete' in construction, so it is reasonably feasible that foamed mortar was used to create the curved coving.

One patent from the time described a method from Aerocrete Foreign Ltd. and Nicol (1928) where 0.1 parts aluminium powder and 0.01 parts stearin were added to 100 parts Portland cement. The aluminium powder reacted with portlandite, releasing hydrogen gas that created large pores (Tang Van et al. 2019). This technique, or a similar method, may have been applied but there is insufficient evidence to confirm the foam used. Results demonstrate that the foamed mortar mix was unlikely to be a mix using 100 parts Portland cement, as the EDX has elevated sillcon and aluminium contents. High aluminium may be explained in part by aluminium powder, but not enough to increase the observed aluminium content from a typical 2.1% by weight in Portland cement to the 10.9% observed (Martínez-Alanis and López-Urías 2016). It is possible that a high alumina cement was used, but the XRD,

Raman, and TGA could not confirm this. Exploratory FE-SEM imaging of the foamed mortar revealed the high sillcon content was due to silica fume particles. The pozzolanic silica fume was added to increase the compressive and flexural strength of the foamed mortar, mitigating the loss of strength due to high porosity and absence of large aggregate (Zhang et al. 2022).

The drilling powder sample showed that the foamed mortar was not representative of the structural concrete. The structural concrete, which was present from 40 mm behind the mosaic surface to the crawl space at 220 mm deep, was created using a cement binder with quartz aggregate. This layer appeared consistent in video surveys with no visible voids (Format NDT LTD 2018). There was no evidence of any carbon-based materials within the mosaic build-up in the videos or laboratory data.

Conclusions

The Freemasons' Hall, which was built in 1927–1933, is a steel-framed Art Deco building containing a large mosaic coving in its Grand Temple. The mosaic was designed by George Murray. Historic records confirmed the mosaic was installed using the indirect method.

The tesserae samples were confirmed to be handmade lead glass produced in Italy by Gino Avon who taught at the world renowned Fruili Mosaic School. This greatly increased the architectural interest of the mosaic, as it was created and installed by a well revered Italian mosaic artist during a time when art exports were being limited. The gold tessera was an ancient Roman style gold leaf glass that used 24-carat gold. Analysis revealed that a thin glass protective layer, the *cartellina,* was made first. The gold leaf was added, followed by a poured lead glass base. The retained gold lustre in the gold glass portions of the mosaic demonstrates that the *cartellina* has protected the gold leaf. Historic images prove that the faded gold portions were not originally designed to be gold and were gilded later, around 1935.

Cementation Index values indicte the thin-set and grout were moderately to eminently hydraulic whilst the bedding coat had hydraulicity above a natural cement. Raman spectroscopy, EDX, XRD, and TGA/DSC results demonstrate that the same mix was employed for both the thin-set and the grout. The Freemasons' Hall's Clerk of Works records from 1932 confirms that the same mix was used for the thin-set and grout and that the bedding coat was a more hydraulic mortar with only cement as the binder whilst the thin-set and grout had a lower hydraulicity cement-lime binder.

Cementation Index values identified that the foamed mortar was an atypical mix. Imaging revealed a highly porous structure containing silica fume that was likely foamed mortar. Foamed mortar was first patented in 1923, so its use in 1932 represents an early use for this material. This greatly enhances the mosaic's architectural interest as it presents a unique situation where authentic mosaic materials produced using historic methods have been combined with newer construction technology including foamed mortar and a steel framed superstructure.

Acknowledgements

The authors wish to thank Tessa Hunkin for helpful advice and discussions when investigating the mosaic craftsmen. Thanks are also due to Susan Snell, Louise Pichel, and their colleagues at the Museum of Freemasonry for arranging and facilitating a visit to study the museum's archives and for arranging copyright permission for historical photographs. Thank you also to Dr Olivier Camus and Mathew Ball at the University of Bath, and to Dr Philip Fletcher and Dr Gabriele Kociok-Köhn from the Materials and Chemical Characterisation Facility (MC2) at the University of Bath for technical support (University of Bath, n.d.).

Disclosure statement

No potential conflict of interest was reported by the author(s).

Funding

This study was supported by the United Grand Lodge of England and the EPSRC Centre for Decarbonisation of the Built Environment (dCarb) [grant number EP/L016869/1].

ORCID

Grace A. Morris http://orcid.org/0000-0001-5858-6508
Kevin Briggs http://orcid.org/0000-0003-1738-9692
Richard J. Ball http://orcid.org/0000-0002-7413-3944

References

Adami, A., F. Fassi, L. Fregonese, and M. Piana. 2018. "Image-based Techniques for the Survey of Mosaics in the St Mark's Basilica in Venice." *Virtual Archaeology Review* 9 (19): 1. https://doi.org/10.4995/var.2018.9087.

Aerocrete Foreign Ltd. and Nicol, C. 1928. *Improvements in or Relating to the Production of Porous Concrete and Similar Material*. GB299484 (A).

Allen, G. C., D. D. Edwards, E. Ciliberto, and S. La Delfa. 2008. "The Medieval Mosaics in St Mark's Basilica, Venice." *Building Limes Forum* 15: 8–14.

Anon. 1935. *Photograph 19'8'35*. London: Museum of Freemasonry.

Arcones-Pascual, G., F. Hernández-Olivares, and A. Sepulcre-Aguilar. 2016. "Comparative Properties of a Lime Mortar with Different Metakaolin and Natron Additions." *Construction and Building Materials* 114: 747–754. https://doi.org/10.1016/j.conbuildmat.2016.03.170.

Battiston, S., and J. P. Grossutti. 2019. "When Arts and Crafts Education Meets Fascism: The Friuli Mosaic School, 1922-1943." *History of Education* 48 (6): 751–768. https://doi.org/10.1080/0046760X.2018.1542743.

Boschetti, C., J. Henderson, J. Evans, and C. Leonelli. 2016. "Mosaic Tesserae from Italy and the Production of Mediterranean Coloured Glass (4rd Century BCE-4th Century CE). Part I: Chemical Composition and Technology." *Journal of Archaeological Science: Reports* 7: 303–311. https://doi.org/10.1016/j.jasrep.2016.05.006.

Brill, R. H. 1963. "Ancient Glass." *Scientific American* 209 (5): 120–131. https://doi.org/10.1038/scientificamerican1163-120.

The buildings illustrated. 1933. *The Architects' Journal* 78 (Jul 20): 92.

Bullard, J. W., H. M. Jennings, R. A. Livingston, A. Nonat, G. W. Scherer, J. S. Schweitzer, K. L. Scrivener, and J. J. Thomas. 2011. "Mechanisms of Cement Hydration." *Cement and Concrete Research* 41 (12): 1208–1223. https://doi.org/10.1016/j.cemconres.2010.09.011.

CAN London Ltd. 2012. *Summary of Survey Findings to Grand Temple Ceiling – United Grand Lodge of England*. Northfleet: CAN London Ltd.

Cizer, Ö, C. Rodriguez-Navarro, E. Ruiz-Agudo, J. Elsen, D. Van Gemert, and K. Van Balen. 2012. "Phase and Morphology Evolution of Calcium Carbonate Precipitated by Carbonation of Hydrated Lime." *Journal of Materials Science* 47 (16): 6151–6165. https://doi.org/10.1007/s10853-012-6535-7.

Clerk of Works. 1932. *Masonic Peace Memorial Clerk of Works Diary July 1931 – June 1932*. London: Warrington & Co. The Garrick Press.

Collendani, G. n.d. *Avon Gino (1896-1984) Mosaicist* [Online]. Accessed 5 July 2023, https://www.dizionariobiografico deifriulani.it/avon-gino/.

Cumbers, A. R. 1932. *Popular Scribbling Diary for* 1932.

Dal Bianco, B., and U. Russo. 2012. "Basilica of San Marco (Venice, Italy/Byzantine Period): Non-Destructive Investigation on the Glass Mosaic Tesserae." *Journal of Non-Crystalline Solids* 358 (2): 368–378. https://doi.org/10.1016/j.jnoncrysol.2011.10.006.

Dean, K. J., W. F. Sherman, and G. R. Wilkinson. 1982. "Temperature and Pressure Dependence of the Raman Active Modes of Vibration of a-Quartz." *Spectrochimico Actn* 38 (10): 1105–1108.

Deschamps, T., C. Martinet, J. L. Bruneel, and B. Champagnon. 2011a. "Soda-lime Silicate Glass Under Hydrostatic Pressure and Indentation: A Micro-Raman Study." *Journal of Physics Condensed Matter [Online]* 23 (3): 035402. https://doi.org/10.1088/0953-8984/23/3/035402.

Deschamps, T., C. Martinet, D. De Ligny, J. L. Bruneel, and B. Champagnon. 2011b. "Correlation Between Boson Peak and Anomalous Elastic Behavior in GeO 2 Glass: An In Situ Raman Scattering Study Under High-pressure." *Journal of Chemical Physics [Online]* 134 (23): 234503-1–234503-4. https://doi.org/10.1063/1.3599939.

Eriksson, J. A. 1924. *Procedure for Manufacturing a Porous Portland Cement Building Material*. DK33046C. Denmark.

Esfandiari, J., and P. Loghmani. 2019. "Effect of Perlite Powder and Silica Fume on the Compressive Strength and Microstructural Characterization of Self-Compacting Concrete with Lime-Cement Binder." *Measurement* 147, https://doi.org/10.1016/j.measurement.2019.07.074.

The Evening Telegraph. 1933. "Distinguished Son of Blairgowrie – Death of George Murray." *The Evening Telegraph* 10 February: 9.

Format NDT LTD. 2018. *Visual Examination Report – Video Scope Examination of the Grand Temple Mosaic*.

Gedzevičiute, V., N. Welter, U. Schüssler, and C. Weiss. 2009. "Chemical Composition and Colouring Agents of Roman Mosaic and Millefiori Glass, Studied by Electron Microprobe Analysis and Raman Microspectroscopy." *Archaeological and Anthropological Sciences* 1 (1): 15–29. https://doi.org/10.1007/s12520-009-0005-4.

Hart, S. 2007. "Two: Temple Emanu-El New York City." *Architectural Record* 195 (6): 69–69.

Historic England. 1982. *Freemasons Hall, Camden – 1113218* [Online]. Accessed 21 August 2019. https://historicengland.org.uk/listing/the-list/list-entry/1113218.

Holmes, S., and M. Wingate. 1997. *Building with Lime. First*. London: Intermediate Technology Publications.

Jones, G. O. 1971. "Structural Chemistry of Glass." *Glass*. Second. 10.

Khan, S. U., M. F. Nuruddin, T. Ayub, and N. Shafiq. 2014. "Effects of Different Mineral Admixtures on the Properties of Fresh Concrete." *The Scientific World Journal* 2014, https://doi.org/10.1155/2014/986567.

Lawrence, R. M. H., T. J. Mays, P. Walker, and D. D'Ayala. 2006. "Determination of Carbonation Profiles in non-Hydraulic Lime Mortars Using Thermogravimetric Analysis." *Thermochimica Acta* 444 (2): 179–189. https://doi.org/10.1016/j.tca.2006.03.002.

The Library and Museum of Freemasonry. 2006. *The Hall in the Garden: Freemasons' Hall and its Place in London. First*. Hersham: Lewis Masonic.

Liu, L., C. J. Lv, C. Q. Zhuang, L. Yi, H. Liu, and J. G. Du. 2015. "First-principles Simulation of Raman Spectra and Structural Properties of Quartz Up to 5 GPa." *Chinese Physics B* 24 (12): 127401-1–127401-9. https://doi.org/10.1088/1674-1056/24/12/127401.

Lothenbach, Barbara, P. Durdziński, and K. de Weerdt. 2016. "Thermogravimetric Analysis." In *A Practical Guide to Microstructural Analysis of Cementitious Materials*, edited by K. Scrivener, R. Snellings, and B. Lothenbach, 177–211. Boca Raton: CRC Press.

Martínez-Alanis, M., and F. López-Urías. 2016. "Cement Pastes and Mortars Containing Nitrogen-Doped and Oxygen-Functionalized Multiwalled Carbon Nanotubes." *Journal of Materials* 2016: 1–16. https://doi.org/10.1155/2016/6209192.

Mindess, S., and J. Francis Young. 1981. *Concrete*. Ed. by P.-H. Inc. NJ, 99–100.

Murray, G. 1930. *Design for Freemasons' Hall (Masonic Peace Memorial Building), Great Queen Street, London: Detail of Mosaic Decoration for the Grand Temple Coving Featuring Symbolic Elements and Statues of Soloman and Hiram. RIBApix* [Online]. Accessed 27 January 2022. https://www.ribapix.com/Design-for-Freemasons-Hall-Masonic-Peace-Memorial-Building-Great-Queen-Street-London-detail-of-mosaic-decoration-for-the-Grand-Temple-coving-featuring-symbolic-elements-and-statues-of-Soloman-and-Hira_RIBA36363.

Museum of Freemasonry. 2020. *Tour of Freemasons' Hall, London Museum of Freemasonry* [Online]. *Youtube* [Online]. Accessed 12 May 2022. https://www.youtube.com/watch?v = Do9yXlnXgrs&ab_channel = MuseumofFreemasonry.

Neri, E., and M. Verità. 2013. "Produrre tessere d'oro: bordi di piastra, ricettari, anlisi archeometriche." *XVIII Colloquio AISCOM* (Cremona, 14–17 mars 2012), Tivoli 2013, 491–505.

Netzsch. 2008. *Application Sheet Ceramics – Building Materials Clay*.

Pesce, G. L., I. W. Fletcher, J. Grant, M. Molinari, S. C. Parker, and R. J. Ball. 2017. "Carbonation of Hydrous Materials at the Molecular Level: A Time of Flight-Secondary ion Mass Spectrometry, Raman and Density Functional Theory Study." *Crystal Growth & Design* 17 (3): 1036–1044. https://doi.org/10.1021/acs.cgd.6b01303.

Pugliese, O. Z. 2004. "The Mosaic Ceiling of 1933 at the Royal Ontario Museum and its Craftsmen: The Untold Story."

Studies in the Decorative Arts 11 (2): 59–77. https://doi.org/10.1086/studdecoarts.11.2.40663081.

Rasmussen, S. C. 2012. Introduction. *How Glass Changed the World: The History and Chemistry of Glass from Antiquity to the 13th Century*. *First*, 1–8.

Ricciardi, P., P. Colomban, A. Tournié, M. Macchiarola, and N. Ayed. 2009. "A non-Invasive Study of Roman Age Mosaic Glass Tesserae by Means of Raman Spectroscopy." *Journal of Archaeological Science* 36 (11): 2551–2559. https://doi.org/10.1016/j.jas.2009.07.008.

Rodriguez-Navarro, C., E. Hansen, and W. S. Ginell. 1998. "Calcium Hydroxide Crystal Evolution upon Aging of Lime Putty." *Journal of the American Ceramic Society* 81 (11): 3032–3034. https://doi.org/10.1111/j.1151-2916.1998.tb02735.x.

Schroeder, J., W. Wu, J. L. Apkarian, M. Lee, L. G. Hwa, and C. T. Moynihan. 2004. "Raman Scattering and Boson Peaks in Glasses: Temperature and Pressure Effects." *Journal of Non-Crystalline Solids* 349 (1–3): 88–97. https://doi.org/10.1016/j.jnoncrysol.2004.08.265.

Scrivener, Karen, A. Bazzoni, B. Mota, and J. E. Rossen. 2016. "Electron Microscopy." In *A Practical Guide to Microstructural Analysis of Cementitious Materials*, edited by K. Scrivener, R. Snellings, and B. Lothenbach, 351–418. Boca Raton: CRC Press.

Serrapede, M., G. L. Pesce, R. J. Ball, and G. Denuault. 2014. "Nanostructured Pd Hydride Microelectrodes: In Situ Monitoring of pH Variations in a Porous Medium." *Analytical Chemistry* 86 (12): 5758–5765.. doi:10.1021ac500310j.

Silva, B. A., A. P. Ferreira Pinto, A. Gomes, and A. Candeias. 2020. "Suitability of Different Surfactants as air-Entraining Admixtures for Lime Mortars." *Construction and Building Materials* 256, https://doi.org/10.1016/j.conbuildmat.2020.118986.

Sims. 1931. *Photograph 7253 G*. London: Museum of Freemasonry.

Sims. 1932a. *Photograph 7969 A*. London: Museum of Freemasonry.

Sims. 1932b. *Photograph 7969 C*. London: Museum of Freemasonry.

Singmaster, D. 1998. "Shanghai Surprises." *The Architects' Journal* 207: 56–57.

Stubbs, J., and T. O. Haunch. 1983. *Freemasons' Hall: The Home and Heritage of the Craft*. First. The Library, Art and Publications Committee.

Tang Van, L., D. Vu Kim, H. Ngo Xuan, T. Vu Dinh, B. Bulgakov, and S. Bazhenova. 2019. "Effect of Aluminium Powder on Lightweight Aerated Concrete Properties." *E3S Web of Conferences* [Online], 97. EDP Sciences. https://doi.org/10.1051/e3sconf/20199702005.

Tantawy, M. A., A. M. El-Roudi, E. M. Abdalla, and M. A. Abdelzaher. 2012. "Evaluation of the Pozzolanic Activity of Sewage Sludge Ash." *ISRN Chemical Engineering* 2012: 1–8. https://doi.org/10.5402/2012/487037.

Torréns-Martín, D., L. Fernández-Carrasco, S. Martínez-Ramírez, J. Ibáñez, L. Artús, and T. Matschei. 2013. "Raman Spectroscopy of Anhydrous and Hydrated Calcium Aluminates and Sulfoaluminates." *Journal of the American Ceramic Society* 96 (11): 3589–3595. https://doi.org/10.1111/jace.12535.

Trushina, D. B., T. V. Bukreeva, and M. N. Antipina. 2016. "Size-controlled Synthesis of Vaterite Calcium Carbonate by the Mixing Method: Aiming for Nanosized Particles." *Crystal Growth & Design* 16 (3): 1311–1319. https://doi.org/10.1021/acs.cgd.5b01422.

Wehrmeister, U., A. L. Soldati, D. E. Jacob, T. Häger, and W. Hofmeister. 2010. "Raman Spectroscopy of Synthetic, Geological and Biological Vaterite: A Raman Spectroscopic Study." *Journal of Raman Spectroscopy* 41 (2): 193–201. https://doi.org/10.1002/jrs.2438.

Yoneyama, A., H. Choi, M. Inoue, J. Kim, M. Lim, and Y. Sudoh. 2021. "Effect of a Nitrite/Nitrate-based Accelerator on the Strength Development and Hydrate Formation in Cold-Weather Cementitious Materials." *Materials* 14 (4): 1006–1014. https://doi.org/10.3390/ma14041006.

Zhang, S., X. Qi, S. Guo, L. Zhang, and J. Ren. 2022. "A Systematic Research on Foamed Concrete: The Effects of Foam Content, Fly Ash, Slag, Silica Fume and Water-to-Binder Ratio." *Construction and Building Materials* 339, https://doi.org/10.1016/j.conbuildmat.2022.127683.

Zhao, H. X., Q. H. Li, S. Liu, and F. X. Gan. 2013. "Characterization of Microcrystals in Some Ancient Glass Beads from China by Means of Confocal Raman Microspectroscopy." *Journal of Raman Spectroscopy* 44 (4): 643–649. https://doi.org/10.1002/jrs.4239.

Zhou, G. T., J. C. Yu, X. C. Wang, and L. Z. Zhang. 2004. "Sonochemical Synthesis of Aragonite-Type Calcium Carbonate with Different Morphologies." *New Journal of Chemistry* 28 (8): 1027–1031. https://doi.org/10.1039/b315198k.